International Journal of Mining Science and Technology 29 (2019) 701–709

Contents lists available at ScienceDirect

International Journal of Mining Science and Technology

journal homepage: www.elsevier.com/locate/ijmst

Rock joint coefficients and their computerized classification

Tomáš Ficker

Faculty of Civil Engineering, Brno University of Technology, 60200 Brno, Czech Republic

ARTICLE INFO

Article history:
Received 24 July 2017
Received in revised form 8 November 2017
Accepted 8 July 2019
Available online 12 July 2019

Keywords:
Rock joints
Shear strength
Joint rock coefficients
Numerical indicators
Computerized assessment

ABSTRACT

A computerized method for determining rock joint coefficients is presented. Two relative similarity indicators are introduced to classify surface morphology of rock joints. The classification enables to compare investigated and database rock joints. Such a comparison aims at finding the couple of surfaces that are distinguished by the highest dynamical conformity. The first absolute indicator results from the Fourier matrix and evaluates wavy shapes of surfaces. The second absolute indicator quantifies the heights of surface reliefs and is defined as the root mean square height of the surface outline. Numerical reliability of these indicators is tested within the surface analysis of a series of limestone specimens. Besides the computerized assessment, 25 people have performed visual assessment of these limestone specimens. The results of visual assessments have been statistically processed and compared to the results received from the computerized procedure. The newly introduced absolute indicators have proved to be prospective numerical tools for evaluating joint rock coefficients.

1. Introduction

Recently, a new method for roughness assessment of rock joints has been outlined [1]. The method has been designed as a fully computerized procedure whose scenario resembled the visual method published by Barton and Choubey [2,3]. In that computerized method, visual assessment was replaced by numerical assessment realized by two similarity indicators. In that method, both the similarity indicators were represented by the relative unitless ratios that however were occasionally numerically unstable and, in addition, the used relative forms proved to be conceptually problematic.

In the present contribution, a new version of the computerized method is developed. In this method, the absolute similarity indicators are employed instead of the relative ones. The absolute indicators provide a non-problematic conceptual solution and show better numerical stability. The present study illustrates functionality of the new absolute indicators and describes all necessary steps that precede, accompany and accomplish the new computational procedure. The hardware and software of the new procedure have been modified to be capable of processing larger rock species, whose linear dimensions equal those implemented in the Barton and Choubey standard visual method [2,3].

The continual interest in roughness coefficients of rock joints is caused by the fact that the surface roughness of rock joints considerably influences the mechanical stability of rock masses. Sufficient stability of rock masses is a prerequisite for the mechanical stability of large civil engineering structures, such as tunnels, dams or bridges situated in regions where the rock masses contain discontinuities. Joints, faults, shear zones, bedding surfaces or foliations are some of the discontinuities that may cause structural weakness of rock masses. In the majority of cases, the stress level due to gravity loads is smaller than the compressive strength of rocks; thus, there is little tendency for intact rocks to fracture. However, the discontinuities situated within steep slopes show a tendency to sliding. Shear strength rather than compressive strength is therefore decisive for stabilizing rock masses. For this reason, the assessment of the shear strength of rock discontinuities is crucial. Several factors influence shear strength: geometry of discontinuities, surface irregularities, physical properties of adjacent rocks, infilling materials, and groundwater are some of them. It is not trivial to decide which one is most important. The fact is that the surface irregularity of rock joints is one of the most important factors. Rock joints are often planar and mostly form a space network embedded into rock masses (Fig. 1).

In geotechnics, there is a long-lasting interest in the surface morphology and shear strength of rock joints. Several models for calculating shear strength exist. These models take into account asperities as relevant factors influencing shear strength. Patton [4] was probably the first who developed a shear strength model for rough rock joints. His model was based on experiments carried out on saw-tooth triangular asperities. Later on, Ladanyi and Archambault [5] succeeded in developing a model that incorpo-

E-mail address: ficker.t@fce.vutbr.cz

https://doi.org/10.1016/j.ijmst.2019.07.002
2095-2686/

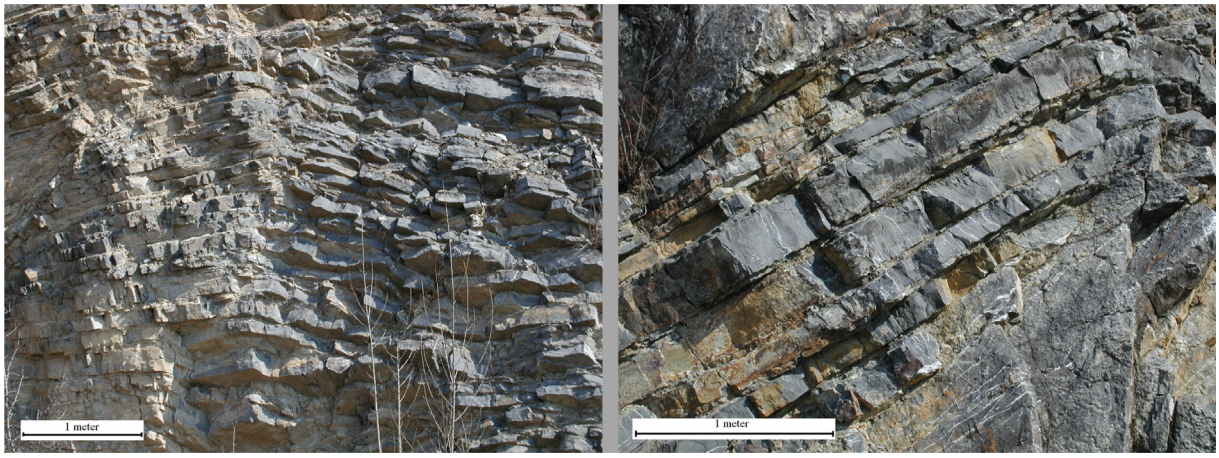

Fig. 1. Networks of rock joints situated in the former lime quarry 'Hády' near the city of Brno in the Czech Republic.

rated the mechanisms of sliding and shearing of asperities into one equation. Kulatilake et al. [6,7] published alternative peak shear strength criteria for rock joints. Their empirical model for peak shear strength is multi-parametric and takes into account the directional dependence of the shear strength.

Barton's [2] model is one of the most frequently used models in geotechnical practice. Barton and Choubey [3] showed experimentally that the shear strength of rock joints τ depends strongly on the asperities of adjacent surfaces, as follows:

$$\tau = \sigma_n \, tg\left[R_{JRC}\log\left(\frac{\sigma_o}{\sigma_n}\right) + \Phi_b\right] \tag{1}$$

where R_{JRC} is the so-called joint roughness coefficient (*JRC*), σ_n the normal effective stress, σ_o the effective joint wall compressive strength (*JCS*) and Φ_b the basic friction angle (i.e. the material constant). The complexity of evaluating τ consists of the complexity of determining R_{JRC}. The joint roughness coefficient R_{JRC} has not assumed an exact analytical expression that would show acceptable performance in all the cases where the joint surfaces may manifest themselves. Barton and Choubey [3] suggested calculating R_{JRC} as follows:

$$R_{JRC} = \frac{arctg\left(\frac{\tau}{\sigma_n}\right)}{\log\left(\frac{\sigma_o}{\sigma_n}\right)} \tag{2}$$

In addition, they proposed a system of 10 reference graphical surface patterns together with the corresponding joint roughness coefficients $R_{JRC} \in (0, 20)$. These standard patterns of known R_{JRC} values enable visual assessment of surface irregularities of rock joints. This visual assessment may be rather subjective, but is often used as a rapid and approximate tool for determining R_{JRC} values.

A good overview of various methods for measuring and quantifying the joint roughness coefficients in current geotechnical practice has been published by Morelli [8]. A comprehensive overview of existing empirical fitting patterns for *JRC* can be found in the two recently published papers by Li and Zhang [9] and Li and Huang [10]. In the first paper Li and Zhang summarize those patterns which employ various measurable topographic parameters. The second paper by Li and Huang summarizes existing empirical fitting patterns for *JRC* that are based on the fractal dimensions D of the measured profiles of jointed surfaces. Other two papers concerning behaviour of rock joints have appeared only recently [11,12].

Besides the joint roughness coefficients, associated with the Barton visual method, there are various other roughness coefficients that can characterize surface irregularities [13–17], but the joint roughness coefficients specified by Eq. (2) are very special indicators derived from experimental measurements of shear strength defined by Eq. (1). This makes them optimally adapted for geotechnical purposes.

Soon after Barton's *JRC* concept [3] had been published, some followers appeared who tried to express the coefficients R_{JRC} in various analytical forms [18–21] using regression procedures. Although many of the suggested regression patterns provide good results, the Barton visual assessment of joint roughness coefficients remains the most frequently used method in geotechnical practice.

The visual comparative method proposed by Barton [2] employs the measured roughness coefficient R_{JRC} assigned to each standard two-dimensional (2D) database profile. The measured *JRC* values represent one great advantage of this method, since measured data are usually closer to reality than those generated by theoretical models. However, visual comparison of surfaces with the standard patterns seems to be rather problematic. When several people perform visual comparisons, it can hardly be expected that they all will come to identical results. The results will be statistically scattered more or less around an average value. To attain a reliable average value of R_{JRC}, it is desirable to ask more people for their judgments (i.e. to use a larger statistical ensemble). However, there are other possibilities as to how to avoid subjectivity in the visual method. One of these possibilities is a computerized assessment based on image recognition, which seems to be a promising solution.

Employment of the Fourier formalism for classifying surface shapes is not a new idea in the field of geotechnics. Fourier shape descriptors have been used for classifying morphological features of granular materials for several decades [22–27]. In particular, sedimentologists have developed various methods for the assessment of surface morphology of microscopic grains. An interesting application of the Fourier analysis to digital imaging of particle shapes has been published by Wettimuny and Penumady [26].

So far, the great majority of studies have concerned microscopic single grains investigated prevalently in 2D regimes. To the best of our knowledge, there is a lack of Fourier shape studies concerning macroscopic 3D surface reliefs of large rock specimens. Since Barton's visual method is based on the shape comparison between larger rock surfaces, its computerized counterpart should also be capable of processing larger species. This study aims at optimizing such a method. Proper numerical indicators of surface similarities should be the core of that method. Finding such indicators is not a straightforward matter, and requires thorough tests that are described here.

2. Scanning 3D surfaces

As has been mentioned, the shape classification of 3D objects requires their scanning and conversion into digital forms. To scan digitally 3D reliefs of larger rock samples (10 cm × 6.67 cm), a special photographic technique has been employed. It uses horizontal optical sections made by the camera, movable in the vertical direction, above the investigated surface (see Fig. 2). To copy the surface, it is necessary to record many optical sections (i.e. digital images taken in discrete vertical positions). A typical number of sections amounts to about 200 images. Optical sections serve as input data for the special software that forms the discrete 3D relief $f(x_i, y_i)$. To suppress the possible data nonlinearity and nonstationarity, pre-processing procedures have been incorporated into the software like polynomial fitting and subtracting the global trend from the profile data along with removing noise by means of averaging the multiplicatively taken snapshots.

One may ask a question as to whether the used sectional reconstruction method shows a quality comparable with other digital methods, e.g. with the scanning laser systems. A detailed study comparing the sectional method with the scanning laser system has been recently reported [27,28]. This study documented that the results of the sectional method were comparable with those of the laser scanning system. One of the many 3D reliefs formed by the sectional method is shown in Fig. 3.

The hardware used for capturing optical sections consists of the photographic camera Canon EOS 600D augmented by the objective EF 100 mm f/2.8 Macro USM (Fig. 2). This objective possesses a sufficiently small depth of optical field when it is set to f/2.8. The photographic camera is mounted on a tough aluminum stand with a stepping motor, enabling discrete movement in the vertical direction. The movement consists of equidistant positions at which the

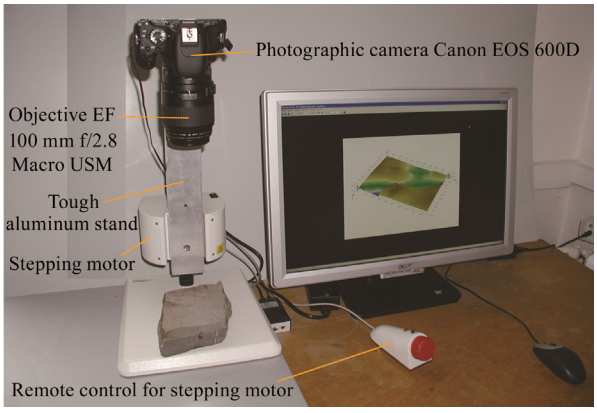

Fig. 2. A laboratory scanning device for capturing 3D surface reliefs.

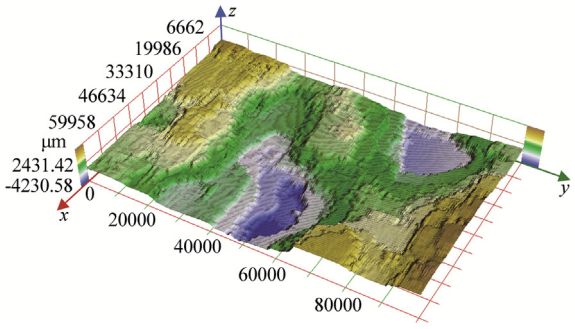

Fig. 3. A scanned relief of limestone surface 10 cm × 6.67 cm with a resolution of 720 pixels × 480 pixels.

Fig. 4. A modified optical device adapted for terrain scanning.

camera takes snaps of the surface. The distance between two positions has to be set so that it may not exceed the depth of the optical field of the objective. The depth of the optical field should be at least several times smaller than the average height of the surface protrusions, or the average depth of the surface depressions.

The developed hardware is usable not only in laboratories but also in outdoor terrain. The photographic camera mounted on an assembly of two tripods and equipped with a proper stepping mechanism may take snaps of large parts of rock reliefs directly in outdoor spaces as shown in Figs. 4 and 5.

3. Fourier 3D reliefs of rock joints

For the morphology analyses of rock joints, the Fourier scheme is proposed. Provided that a 3D surface relief is available in a discrete scanned form $f(x_i, y_i)$, it can be fitted by the Fourier partial sum:

$$f(x_i,y_j) \approx F_N(x_i,y_j) = \sum_{k,n=0}^{N-1} \tau_{kn}\left(a_{kn}\cos\frac{k\pi x_i}{p}\cos\frac{n\pi y_j}{q} + b_{kn}\sin\frac{k\pi x_i}{p}\cos\frac{n\pi y_j}{q} + c_{kn}\cos\frac{k\pi x_i}{p}\sin\frac{n\pi y_j}{q} + d_{kn}\sin\frac{k\pi x_i}{p}\sin\frac{n\pi y_j}{q}\right) \quad (3)$$

where,

$$\Omega = \{x \in (-p,+p),\ \ y \in (-q,+q)\} \quad (4)$$

$$a_{kn} = \frac{1}{pq}\iint_\Omega f(x,y)\cos\frac{k\pi x}{p}\cos\frac{n\pi y}{q}dxdy \quad (5)$$

$$b_{kn} = \frac{1}{pq}\iint_\Omega f(x,y)\sin\frac{k\pi x}{p}\cos\frac{n\pi y}{q}dxdy \quad (6)$$

$$c_{kn} = \frac{1}{pq}\iint_\Omega f(x,y)\cos\frac{k\pi x}{p}\sin\frac{n\pi y}{q}dxdy \quad (7)$$

$$d_{kn} = \frac{1}{pq}\iint_\Omega f(x,y)\sin\frac{k\pi x}{p}\sin\frac{n\pi y}{q}dxdy \quad (8)$$

$$\tau_{kn} = \begin{cases} 1 & k>0,\ n>0 \\ 1/2 & k=0,\ n>0 \quad or \quad k>0,\ n=0 \\ 1/4 & k=n=0 \end{cases} \quad (9)$$

The symbol N defines the upper bound (N-1) for the subscripts n, k, and restricts the number of terms in the Fourier partial sum specified by Eq. (3).

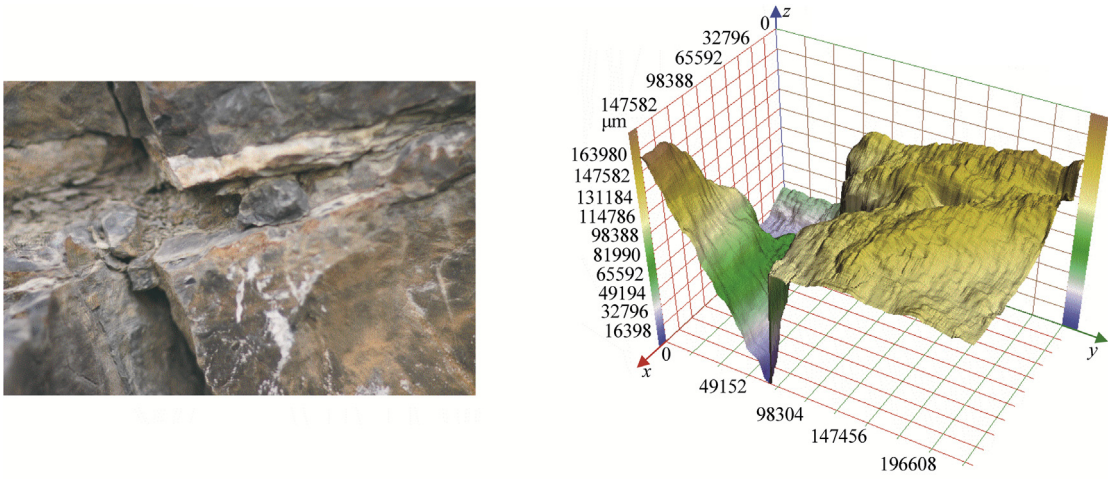

(a) Photography of the original rock relief

(b) Three-dimensional copy of the terrain relief reproduced by the sectional method

Fig. 5. Rock relief scanned in terrain (After [28,29]).

To develop a corresponding mathematical basis for the Fourier indicators of 3D reliefs, it is convenient to rewrite Eq. (3) as follows:

$$f(x_i,y_j)\approx\sum_{k,n=0}^{N-1}\left[\alpha_k\cos\frac{k\pi x_i}{p}+\beta_k\sin\frac{k\pi x_i}{p}\right]\cdot\left[\gamma_n\cos\frac{n\pi y_j}{q}+\delta_n\sin\frac{n\pi y_j}{q}\right] \tag{10}$$

where,

$$\begin{cases}\alpha_k\gamma_n=\tau_{kn}\cdot a_{kn}\\ \beta_k\gamma_n=\tau_{kn}\cdot b_{kn}\\ \alpha_k\delta_n=\tau_{kn}\cdot c_{kn}\\ \beta_k\delta_n=\tau_{kn}\cdot d_{kn}\end{cases} \tag{11}$$

Eq. (10) contains a product of two terms in brackets. These terms represent harmonic waves with characteristic wavelengths $\lambda_x = 2p/k$ and $\lambda_y = 2q/n$ (in pixels). The functional products specified by Eq. (10) represent 2D wave modes possessing indices (k, n) and wavelengths (λ_x, λ_y). A square matrix $\boldsymbol{M}_N$ of the Fourier indicators $D_N(k,n)$ may be introduced as follows:

$$M_N=\begin{pmatrix}D_N(0,0) & D_N(0,1) & \cdots\cdots & D_N(0,N-1)\\ D_N(1,0) & D_N(1,1) & \cdots\cdots & D_N(1,N-1)\\ & & \cdots\cdots & \\ & & \cdots\cdots & \\ D_N(N-1,0) & D_N(N-1,1) & \cdots\cdots & D_N(N-1,N-1)\end{pmatrix} \tag{12}$$

$$D_N(k,n)=\sqrt{(\tau_{kn}\cdot a_{kn})^2+(\tau_{kn}\cdot b_{kn})^2+(\tau_{kn}\cdot c_{kn})^2+(\tau_{kn}\cdot d_{kn})^2} \tag{13}$$

Some of the matrix elements have special meanings. For example, the first element $D_N(0,0) = a_{0,0}/4$ is associated with an infinitively large wavelength and represents a basic height of the horizontal level. Its value will be the largest compared to all other matrix elements. From the viewpoint of the shape (wave) analysis, this first diagonal element is irrelevant and will be set to zero. It will not be taken into account in further consideration. The matrix $\boldsymbol{M}_N$ is a characteristic matrix and contains all relevant wave modes of surface reliefs. One example of this matrix plotted in graphical form as a function of two variables k, n is presented in Fig. 6.

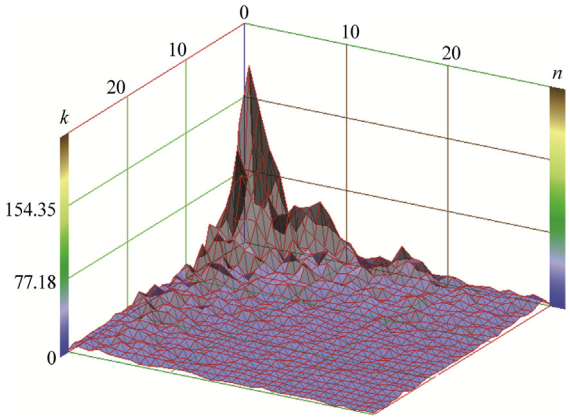

Fig. 6. An example of the graphical output of the Fourier matrix $\boldsymbol{M}_N(k,n)$.

Naturally, it would be possible to study each particular indicator $D_N(k,n)$ or groups of indicators, and to reveal their functionality associated with local morphological features of 3D reliefs. Undoubtedly, the indicators of lower orders ($k,n < 10$) bear information on a global wavy shape of the relief, since they correspond to spatial waves of large wavelengths (i.e. small frequencies). The indicators of higher orders ($k,n > 10$) would undoubtedly quantify a finer structure of 3D reliefs. All these properties can be observed on the graphical plot of the matrix $\boldsymbol{M}_N$ in Fig. 6, where the indicators of lower orders manifest large values (peak values), whereas the indicators of higher orders quickly lose their magnitudes. However, a detailed analysis of this kind would not be practical. One-valued indicators enabling quick orientation and a rapid decision are needed. To reach this goal, reformulating the matrix $\boldsymbol{M}_N$ is necessary. This task is accomplished in the next section.

4. Classifying surface morphology

Prior to selecting similarity indicators, it must be clear which surface features should be compared and what should actually be understood under the notion of 'surface similarity'. Only surface features that are decisive for the shear strength of rock joints have to be preferably taken into account. Barton and Choubey [2,3] divided surfaces of rock joints into 10 categories according to their

morphologies, starting from planar and smooth surfaces up to wavy and rough surfaces. Likewise, Bandis [30] described a set of surfaces according to their morphologies, and mentioned three basic shape categories, namely planar, undulating and stepped surfaces. He divided each category into three height subcategories, namely the subcategories that he termed as slickensided, smooth and rough. These categories and subcategories are mutually independent and may be combined into nine different morphological patterns. Naturally, this is a simplified classification and, in reality, further variants of surface profiles may appear. However, even from this simplistic distribution, it is clear that the shape and height of the surface profiles are two relevant surface features that are decisive in the assessment of the shear strength of rock joints. These characteristics also play an important role in evaluating the similarity of rock joint surfaces.

However, under the term 'similarity' cannot be understood a simple geometrical similarity since jointed surfaces show specific dynamical properties resulted in shear strength that is directionally dependent. Consequently, the corresponding shape indicator should be sensitive to the direction of shearing, i.e., it should be rotationally sensitive. Such an indicator is capable of classifying the so called 'dynamical similarity' of jointed surfaces. On the other hand, the global heights of 3D profiles are independent of directions and thus the corresponding height indicator should be invariant of rotations. It is necessary to find at least two independent indicators, one of which will classify shape (planarity, waviness, stepped shape, etc.) and will be rotationally sensitive whereas the second will classify profile height and will show invariance of rotation. The matrix $\boldsymbol{M}_N$ seems to be a good starting point for forming a one-valued shape indicator, since this matrix contains 'signatures' of all characteristic wave modes of the surfaces. As a height indicator, the so-called root mean square (RMS) parameter R_q might be convenient, since it evaluates global heights of surface profiles. This global indicator is frequently used when analyses of surface roughness are performed [13–17].

For the purpose of comparison of jointed surfaces, the following two absolute numerical indicators S, and H will be employed. The first indicator S is derived from the elements $D_N(k,n)$ of the Fourier matrix $\boldsymbol{M}_N$ as a true indicator of dynamical similarity; and the second indicator H quantifies the global invariant heights of 3D surface profiles:

$$S(N) = \sum_{k=0}^{N-1}\sum_{n=0}^{N-1} |D_N^{(0)}(k,n) - D_N(k,n)| \tag{14}$$

$$H(N) = |R_q^{(o)}(N) - R_q(N)| \tag{15}$$

$$R_q(N) = \sqrt{\frac{1}{K\cdot L}\sum_{i=1}^{K}\sum_{j=1}^{L}\left[f(x_i,y_j) - F_N^{(low)}(x_i,y_j)\right]^2} \tag{16}$$

where $f(x_i, y_j)$ is the scanned relief and $F_N^{(low)}(x_i, y_j)$ represents the Fourier relief, which serves as a basis for computing height differences. The auxiliary quantities $R_q(N)$ and $R_q^{(o)}(N)$are *RMS* values related to the tested surface and the database surface, respectively. The symbols $D_N(k, n)$ and $D_N^{(o)}(k,n)$ in Eq. (14) are associated with the tested surface and the database surface, respectively. The product $K{\cdot}L$ is a pixel resolution of the used digital images of surfaces. In our case $K{\cdot}L$ = 720 pixels × 480 pixels (the color pixel raster of the CMOS sensor of the camera), which corresponds to the area 10 cm × 6.67 cm (measured on the samples). The symbol $f(x_i, y_j)$ in Eq. (16) represents the scanned relief.

In the first phase of the morphology research of jointed surfaces, we tried to find numerical indicators independent of measuring techniques in order the results coming from different laboratories could be comparable. From this viewpoint, the relative indicators introduced as fractions in which the numerators had absolute forms (see Eqs. (14) and (16)) whereas the denominators contained the database terms $D_N^{(o)}(k,n)$ and $R_q^{(o)}(N)$, respectively, seemed to be convenient [1]. However, further research showed that relative indicators are not as numerical stable as the absolute indicators specified by Eqs. (14) and (16) and, in addition, the denominators may occasionally change the right predictions of absolute numerators. In other words, the relative indicators are not as reliable as the absolute indicators. For this reason, we have abandoned the relative indicator forms in the present paper and introduced the absolute indicators defined by Eqs. (14) and (16) as convenient parameters that are capable of revealing dynamical similarities of jointed surfaces more reliably. Further detailed discussion concerning functional behaviour of the absolute numerical indicators and their properties can be found elsewhere [31].

It should be highlighted that the jointed surfaces acquired by drilling the terrain slopes usually show some artificial base that is often inclined or bended. This additional unwanted parts of joints represent functional trends which are not inherent parts of joints and have to be removed. These functional trends can be fitted by the Fourier profiles with sufficiently low N-values, i.e. $F_N^{(low)}(x_i, y_j)$or by the two-dimensional polynomials. These fitted discrete functions serve as reference levels and are employed for correcting the scanned profiles (reliefs) $f(x_i,y_j)$ as shown in Eq. (16).

When computing the Fourier matrix specified by Eq. (12), the corrected scanned profile has to be used as well, i.e.

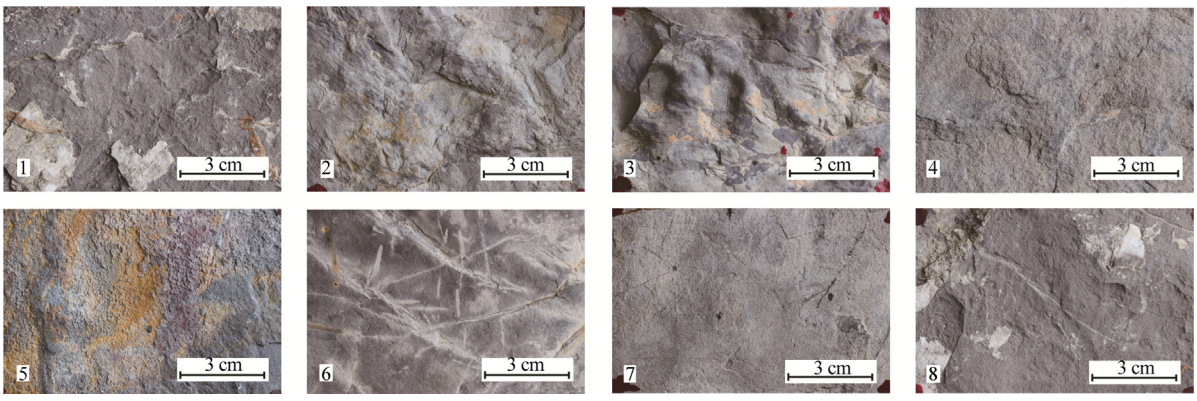

Fig. 7. Eight limestone species of various surface textures selected for similarity tests.

$[f(x_i,y_j) - F_N^{(low)}(x_i,y_j)] \rightarrow f^{(corrected)}(x_i,y_j)$. This corrected scanned function is then used for computing the accurate matrix $D_N(k,n)$, but this time it is necessary to perform the Fourier expansion with a sufficiently high N-value to faithfully describe all the surface irregularities including wavy shapes and asperity structures.

Since the root-mean-square height indicator H is calculated according to Eqs. (15) and (16) as a difference between the reference level $F_N^{(low)}(x_i,y_j)$ and the scanned relief $f(x_i, y_j)$, i.e. as a two-level difference, the indicator H is independent of rotation. The required sensitivity of the indicator S to the operations of rotation deserves a detailed discussion and can be found in Ref. [31]. Both the indicators S and H fulfill the necessary properties for correct assessing the dynamical conformity of three-dimensional reliefs.

Table 1
Visual and computer assessments.

Investigated surface	Visual assessment	Computer assessment	
	The most similar database surfaces	The most similar database surfaces	
		S	H
1	4	4	4
2	3 and 8	8	8
3	2	2	2
4	1	1	1
5	8	8	8
6	7	7	7
7	6	6	6
8	5 and 2	5	5

Eqs. (14)–(16) should be capable of identifying such a database relief that shows the highest dynamical conformity with the relief under investigation. When two identical reliefs are compared, a full conformity (dynamical similarity) must be indicated, and the two indicators have to show zero values ($S = 0$, $H = 0$). Such a situation can only rarely occur in practice when two independent reliefs are compared. In the great majority of situations, only incomplete dynamical similarity will be found, which will be indicated by some minimum positive values of shape and height indicators, i.e. $0 < S$, $0 < H$. In addition, height and geometrical shape are two more or less independent properties and may show a variety of combinations. Accordingly, the indicators S and H may show different results in some situations and in this case the result associated with a smaller value of JRC should be accepted since this value is at the side of higher safety. An analogous problem may arise when a group of people performs visual assessments of rock joints.

The tests in the following section are aimed at the functionality of the indicators S and H.

5. Test of similarity indicators

Eight fragments taken from the former limestone quarry 'Hády' near the city of Brno in the Czech Republic (Fig. 1) have been gathered. Their surfaces (Fig. 7) have diverse morphologies starting from very coarse (No. 3 in Fig. 7) up to very fine (No. 6 in Fig. 7). The fragments do not represent real rock joints, but their surface morphologies cover almost the entire range of Barton's standard profiles [2]. These eight surfaces have been subjected to similarity tests. A particular surface has been compared to the remaining seven surfaces that play the role of database surfaces. This procedure was repeated eight times, i.e., each surface was compared to the rest of the other database surfaces. The comparative procedure

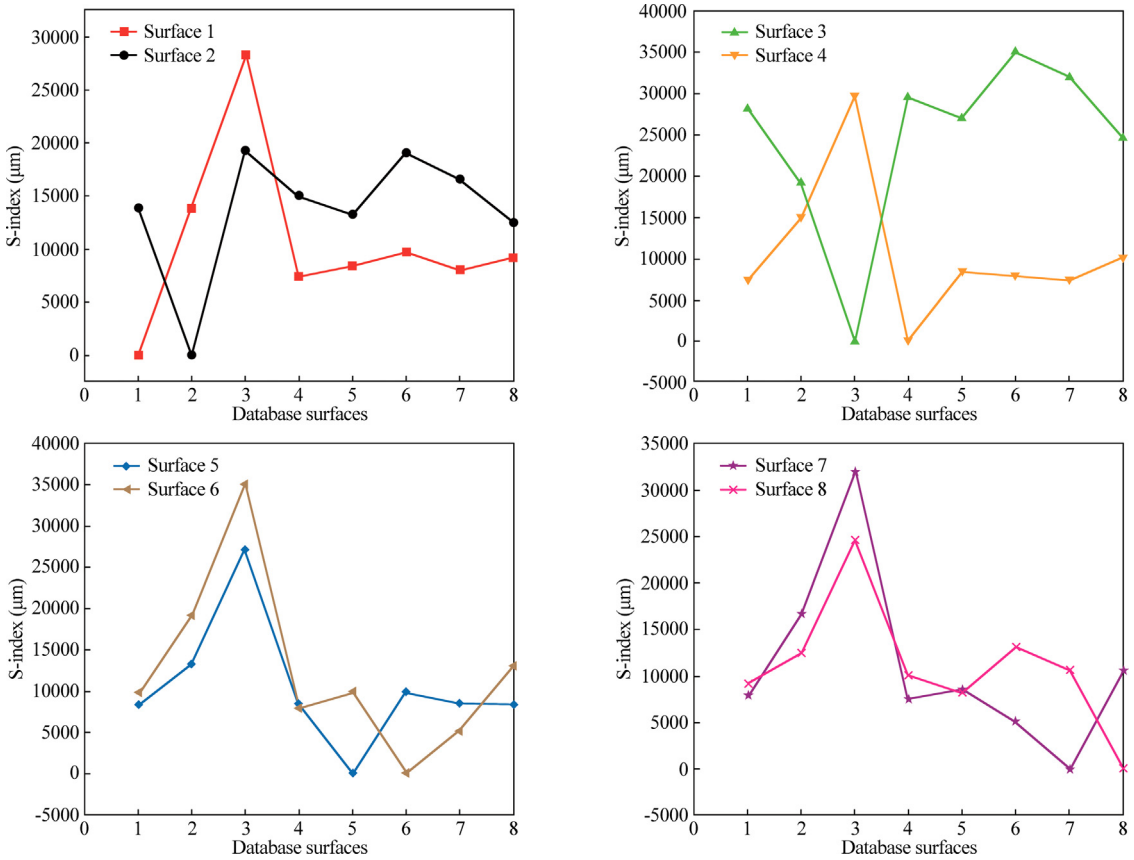

Fig. 8. Values of S-indicators computed for couples of surfaces. The S-indicators have to show zero values when two identical surfaces are compared. The couples of identical surfaces are as follows: 1–1, 2–2, 3–3, 4–4, 5–5, 6–6, 7–7, and 8–8. These simple tests illustrate the correct functionality of the software used.

was performed both visually (subjectively) and automatically (objectively) on the computer.

Similarity comparisons of surfaces are problematic, since there are no tools enabling a decision with absolute certainty. For this reason, we performed a double comparison (i.e. visual and computerized) in order that the results may be confronted.

5.1. Visual assessment

To obtain statistically relevant results, we asked 25 people to classify the surfaces according to the standard profiles of Barton [2,3]. In this way, the corresponding *JRC*-values have been ascribed to surfaces and the couples of the most dynamically similar surfaces have been specified. Naturally, these individual decisions were not unified but rather dispersed. Since it was hardly possible to weight statistically each decision, we calculated common arithmetic averages of *JRC* values and the couples of the most similar surfaces have been saved in Table 1.

It should be highlighted that the visual assessments of rock surfaces based on human judgments are rather problematic, since the results are affected by statistical variability caused by individual human differences.

5.2. Computer assessment

The second type of similarity comparison has been performed on the computer by using indicators *S* and *H*. Scanned surfaces No. 1-No. 8 (Fig. 7) were converted into the corrected Fourier reliefs, from which the descriptor matrices $\boldsymbol{M}_N$ (Eqs. (12) and (13)) were derived, and afterwards the values of the global shape indicator *S* and the height indicator *H* were evaluated.

To verify the functionality of the software, a simple test was carried out. The test was based on comparisons between one chosen surface and the eight 'database' surfaces among which the chosen surface was also present. Within such a comparison, where two identical surfaces can be met, the similarity indicators *S* and *H* have to show full dynamical similarity (zero values). Figs. 8 and 9 show the results of such tests. The graphs in these plots confirm that the software correctly identified all eight couples of identical surfaces.

The main tests are, however, focused on similarity comparisons of non-identical surfaces. An investigated surface was compared to the remaining seven database surfaces. There are eight such arrangements: (i) surface No. 1 versus Nos. 2–8, (ii) surface No. 2 versus Nos. 1 and 3–8, (iii) surface No. 3 versus Nos. 1, 2 and 4–8, (iv) surface No. 4 versus Nos. 1–3 and 5–8, (v) surface No. 5 versus Nos. 1–4 and 6–8, (vi) surface No. 6 versus Nos. 1–5 and 7, 8, (vii) surface No. 7 versus Nos. 1–6 and 8, (viii) surface No. 8 versus Nos. 1–7. All these numerical comparisons were accomplished, and the corresponding graphs are presented in Figs. 10 and 11. In these graphs, the corresponding most similar database surfaces are indicated by bold arrows.

Fig. 10 shows the results of similarity comparisons performed by means of the *S*-indicators. For example, the chosen surface No. 1 is compared to the database surfaces Nos. 2–8; its database counterpart No. 4 was found as its most similar partner among the remaining database surfaces. Accordingly, in Fig. 10, the bold arrow points to the database surface No. 4. Since the comparisons are not performed between identical surfaces, the values of the

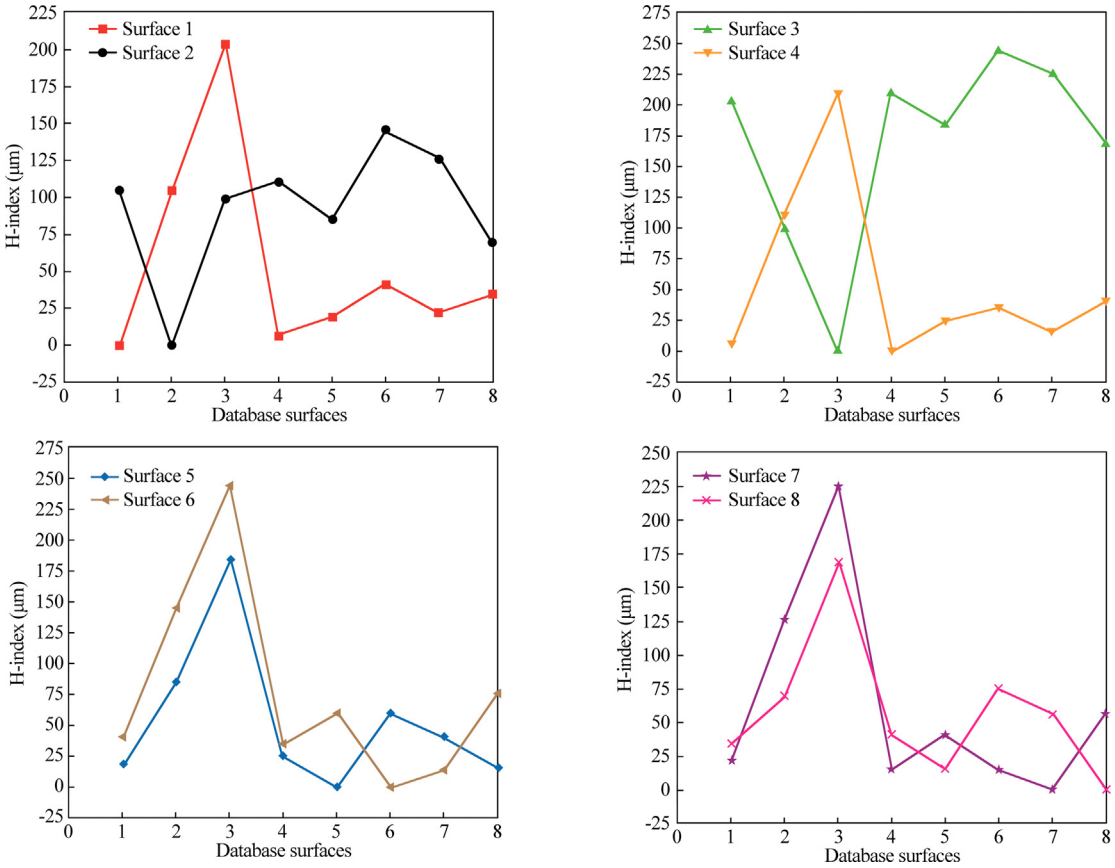

Fig. 9. Values of *H*-indicators computed for couples of surfaces. The *H*-indicators have to show zero values when two identical surfaces are compared. The couples of identical surfaces are as follows: 1–1, 2–2, 3–3, 4–4, 5–5, 6–6, 7–7, and 8–8. These simple tests illustrate the correct functionality of the software used.

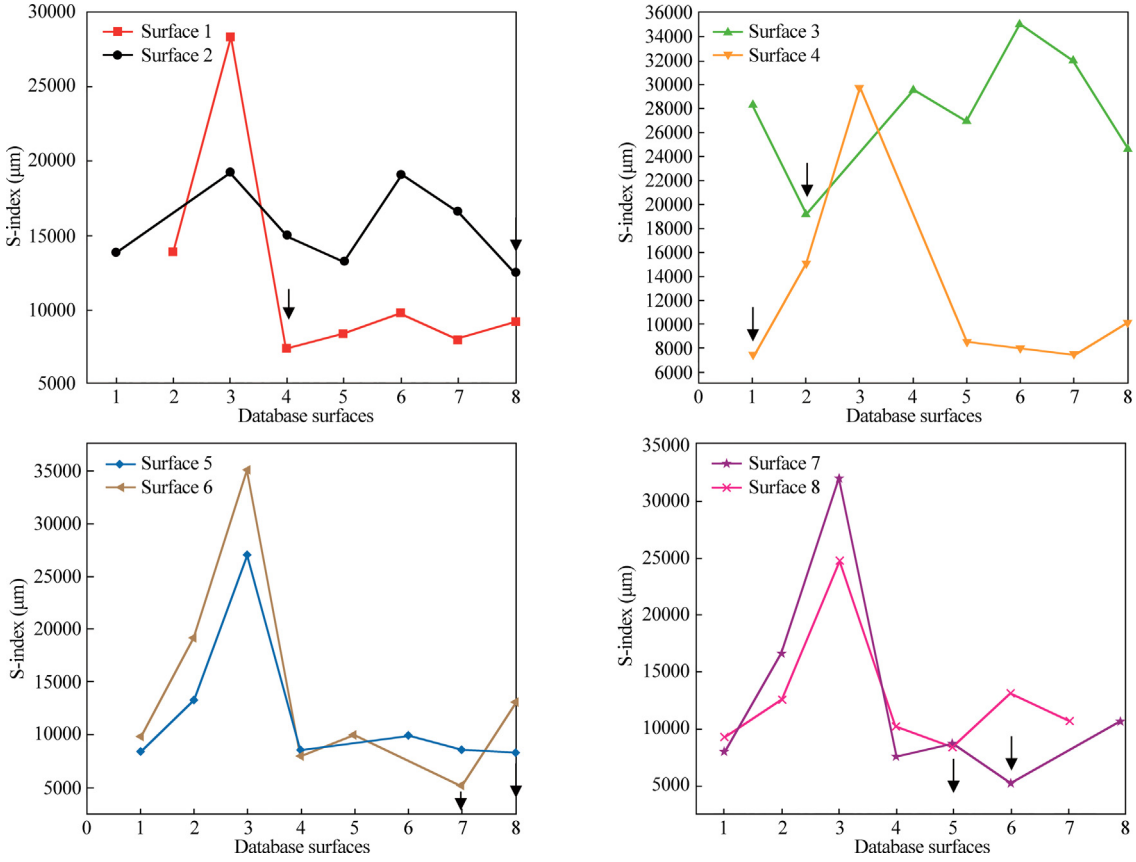

Fig. 10. Computerized similarity tests for non-identical surfaces. Values of *S*-indicators are computed for the following couples: 1 versus 2–8; 2 vs. 1, 3–8; 3 vs. 1, 2, 4–8; 4 vs. 1–3, 5–8; 5 vs. 1–4, 6–8; 6 vs. 1–5, 7, 8; 7 vs. 1–6, 8; 8 vs. 1–7. The arrows point to the most similar database surfaces.

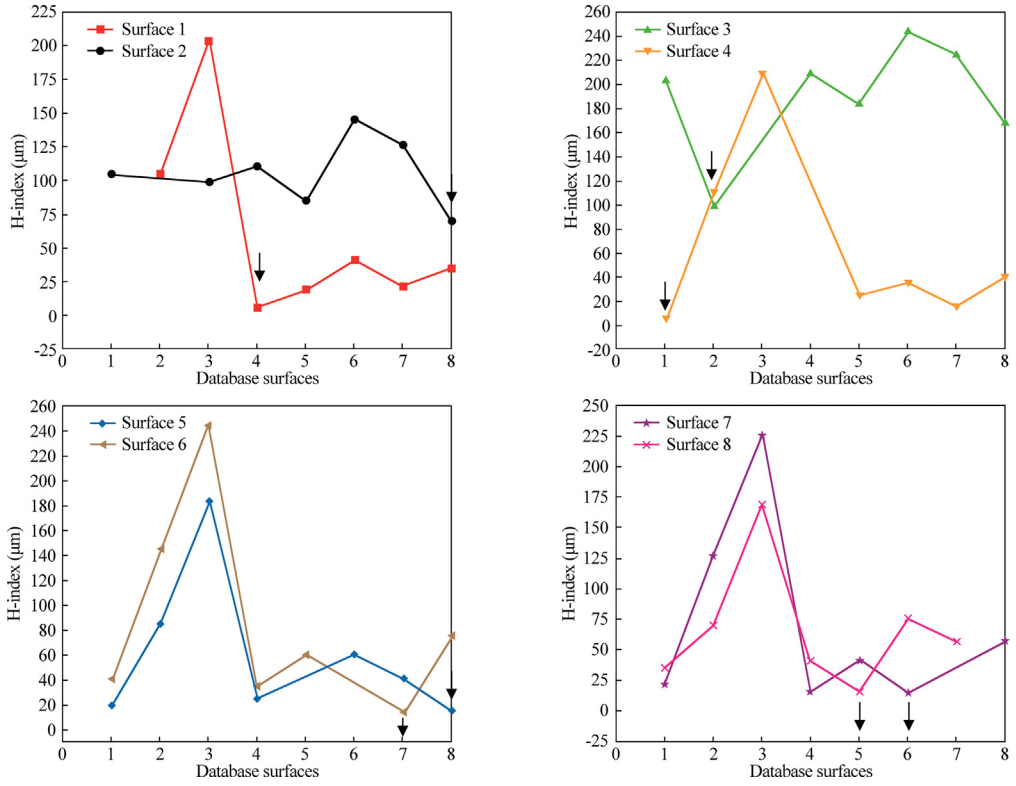

Fig. 11. Computerized similarity tests for non-identical surfaces. Values of *H*-indicators are computed for the following couples: 1 versus 2–8; 2 vs. 1, 3–8; 3 vs. 1, 2, 4–8; 4 vs. 1–3, 5–8; 5 vs. 1–4, 6–8; 6 vs. 1–5, 7, 8; 7 vs. 1–6, 8; 8 vs. 1–7. The arrows point to the most similar database surfaces.

S-indicators cannot be equal to zero, but they show small positive non-zero values, which represent the total minima of the *S*-graphs. The other investigated surfaces (Nos. 2–8) were treated analogously.

Fig. 11 offers results achieved by means of the height *H*-indicators. The arrangement is the same as in Fig. 10, and the bold arrows again point to the most similar database surfaces. All the results of the *H*-indicators shown in Fig. 11 agree with those of the *S*-indicators presented in Fig. 10. The results of the similarity assessments achieved by the two indicators *S* and *H* are collected in Table 1.

5.3. Comparing visual and computer assessments

Table 1 contains the results of both the visual and computer assessments. Both these assessments are in good agreement. The absolute indicators *S* and *H* seem to be convenient for the computerized similarity assessments of rock joints. They constitute principal tools in the developed software code. Although their predictive results have been identical in all our presented tests and in many others so far not published, it should be repeatedly stressed that these two indicators may sometimes slightly differ in their predictions especially when height and shape properties of surface reliefs are not sufficiently correlated. In such cases the smaller *JRC* value should be preferably accepted as a parameter that guarantees higher safety.

The performed tests have shown that the absolute forms of the indicators *S* and *H* have succeeded in their role of similarity indicators finding rock joint coefficients associated with the database reliefs. The modified hardware and software were capable of correctly processing large rock surfaces whose linear sizes were fully comparable to those of the Barton standard *JRC* profiles.

6. Conclusions

The visual assessment of the roughness of rock joints, often used in geotechnical engineering, may be replaced by the fully computerized procedure based on the absolute height *H* and shape *S* indicators. The absolute functional forms of these indicators have proved to be numerically more stable compared to the relative indicators used previously. The computerized procedure based on comparison with the database surfaces of known *JRC* yields two kinds of the rock joint coefficients, namely JRC_H and JRC_S, which are termed according to the indicators *H* and *S*. The values JRC_H and JRC_S are usually identical, especially when there is a higher correlation between the height and wavy shapes of the surface profiles. Nevertheless, a weaker correlation may cause a slight difference between these two coefficients. In such a case, the weighted or simple average $(JRC_H + JRC_S)/2$ may be used but the safest solution is to accept the smaller value of these two magnitudes.

The developed computerized comparative method is applicable not only to the rock joints in geotechnics, but also to other fields of science and technology where surface morphology plays an important role. The method is capable of processing both the microscopic and macroscopic specimens and this makes the method very universal.

Acknowledgments

This work was supported by the Grant Agency of the Czech Republic under contract No. 13-03403S.

References

[1] Ficker T, Martišek D. Alternative method for assessing the roughness coefficients of rock joints. J Comp Civ Eng 2016;30:04015059.
[2] Barton N. Review of a new shear strength criterion for rock joints. Eng Geol 1973;7:87–332.
[3] Barton N, Choubey V. The shear strength of rock joints in theory and practice. Rock Mech 1977;10:1–65.
[4] Patton FD. Multiple modes of shear failure in rock. In: 1st ISRM congress, Lisbon, Portugal. p. 509–15.
[5] Ladanyi B, Archambault G. Simulation of shear behaviour of a jointed rock mass. In: The 11th US rock mechanics symposium, Berkeley, CA. p. 105–25.
[6] Kulatilake PHSW, Shou G, Huang TH, Morgan RM. New peak shear strength criteria for anisotropic rock joints. Int J Rock Mech Min Sci Geomech Abstr 1995;32:673–97.
[7] Kulatilake PHSW, Shou G, Huang TH. Spectral-based peak-shear-strength criterion for rock joints. J Geotech Eng 1995;121:789–96.
[8] Morelli GL. On joint roughness: Measurements and use in rock mass characterization. Geotech Geol Eng 2014;32:345–62.
[9] Li Y, Zhang Y. Quantitative estimation of joint roughness coefficient using statistical parameters. Int J Rock Mech Mining Sci 2015;77:27–35.
[10] Li Y, Huang R. Relationship between joint roughness coefficient and fractal dimension of rock fracture surfaces. Int J Rock Mech Mining Sci 2015;75:15–22.
[11] Saeid DR, Elnaz SI. A modified model of a single rock joint's shear behaviour in limestone specimens. Int J Mining Sci Technol 2016;26:577–80.
[12] Yang XX, Jing HW, Chen KF. Numerical simulations of failure behaviour around a circular opening in a non-persistently jointed rockmass under biaxial compression. Int J Mining Sci Technol 2016;26:729–38.
[13] Ficker T, Martišek D, Jennings HM. Roughness of fracture surfaces and compressive strength of hydrated cement pastes. Cem Concr Res 2010;40:947–55.
[14] Ficker T, Martišek D. Roughness and fractality of fracture surfaces as indicators of mechanical quantities of porous solids. Central Europ J Phys 2011;9:1440–5.
[15] Ficker T, Martišek D, Jennings HM. Surface roughness and porosity of hydrated cement pastes. Acta Polytech 2011;51:7–20.
[16] Ficker T. Fracture surfaces of porous materials. Acta Polytechnica 2011;51:21–4.
[17] Ficker T. Fracture surfaces and compressive strength of hydrated cement pastes. Constr Build Mater 2012;27:197–205.
[18] Tse R, Cruden DM. Estimating joint roughness coefficients. Int J Rock Mech Min Sci Geomech Abstr 1979;16:303–7.
[19] Maerz NH, Franklin JA, Bennett CP. Joint roughness measurement using shadow profilometry. Int J Rock Mech Min Sci Geomech Abstr 1990;27:329–43.
[20] Hong ES, Lee IM, Lee JS. Measurement of rock joint roughness by 3D scanner. Geotech Testing J 2006;2006(29):1–8.
[21] Hong ES, Lee IM, Lee JS. Underestimation of roughness in rough rock joints. Int J Numer Anal Meth Geomech 2008;32:1385–403.
[22] Ehrlich R, Weinberg B. An exact method for characterization of grain shape. Sediment Petrol 1970;40:205–12.
[23] Clark MW. Quantitative shape analysis: a review. Math Geol 1981;4:303–20.
[24] Thomas MC, Wiltshire RJ, Williams AT. The use of Fourier descriptors in the classification of particle shape. Sedimentology 1995;42:635–45.
[25] Bowman ET, Soga K, Drummond W. Particle shape characterisation using Fourier descriptor analysis. Géotechnique 2001;51:545–54.
[26] Wettimuny R, Penumady D. Application of Fourier analysis to digital imaging for particle shape analysis. J Comp Civ Eng 2004;18:2–9.
[27] Ficker T, Martišek D. Three-dimensional reconstructions of solid surfaces using conventional microscopes. J Scann Microsc 2016;38:21–35.
[28] Ficker T. Sectional techniques for 3D imaging of microscopic and macroscopic objects. Optik – Int J Light Electron Optics 2017;144:289–99.
[29] Audy O, Ficker T. Large rock reliefs and their 3D reconstruction. IOP Conf Series: Mater Sci Eng 2017;245.
[30] Bandis SC. Engineering properties and characterization of rock discontinuities. In: Hudson JA, editor. Comprehensive rock engineering: principles, practice and projects. Oxford: Pergamon Press; 1993. p. 155–83.
[31] Ficker T. Some remarks on the dynamical conformity of rock joints. Int J Min Sci Technol 2018;28(3):385–90.